A Gray-Radiation Aquaplanet Moist GCM. Part I: Static Stability and Eddy Scale

DARGAN M. W. FRIERSON

Program in Applied and Computational Mathematics, Princeton University, Princeton, New Jersey

ISAAC M. HELD

NOAA/GFDL, Princeton, New Jersey

PABLO ZURITA-GOTOR

UCAR/GFDL, Princeton, New Jersey

(Manuscript received 14 April 2005, in final form 9 January 2006)

ABSTRACT

In this paper, a simplified moist general circulation model is developed and used to study changes in the atmospheric general circulation as the water vapor content of the atmosphere is altered. The key elements of the model physics are gray radiative transfer, in which water vapor and other constituents have no effect on radiative fluxes, a simple diffusive boundary layer with prognostic depth, and a mixed layer aquaplanet surface boundary condition. This GCM can be integrated stably without a convection parameterization, with large-scale condensation only, and this study focuses on this simplest version of the model. These simplifications provide a useful framework in which to focus on the interplay between latent heat release and large-scale dynamics. In this paper, the authors study the role of moisture in determining the tropospheric static stability and midlatitude eddy scale. In a companion paper, the effects of moisture on energy transports by baroclinic eddies are discussed.

The authors vary a parameter in the Clausius–Clapeyron relation to control the amount of water in the atmosphere, and consider circulations ranging from the dry limit to 10 times a control value. The typical length scale of midlatitude eddies is found to be remarkably insensitive to the amount of moisture in the atmosphere in this model. The Rhines scale evaluated at the latitude of the maximum eddy kinetic energy fits the model results for the eddy scale well. Moist convection is important in determining the extratropical lapse rate, and the dry stability is significantly increased with increased moisture content.

1. Introduction

The model described herein is our attempt to construct an idealized moist general circulation model. It can be thought of as an extension of the dry model of Held and Suarez (1994) to include latent heat release. The Held and Suarez (1994) model consists of the standard primitive equation dynamical core, along with Newtonian cooling to a specified radiative equilibrium profile, and Rayleigh damping to represent the surface boundary layer. The model was proposed as a benchmark for the systematic comparison of GCM dynamical cores, but its climatology qualitatively resembles that of the atmosphere, and it has been used for a number of dynamical studies, including Franzke (2002), Seager et al. (2003), Williams (2003), Kushner and Polvani (2004), Harnik and Chang (2004), and Franzke et al. (2004).

In designing an idealized moist general circulation model, our goal has been to create a framework to which we can sequentially add the various components of a full atmospheric GCM, and to have some flexibility in the choice of a lower boundary condition. To this end we have included an explicit boundary layer model and replaced the Newtonian cooling with a very simple gray radiative model that predicts upward and downward fluxes. In this study we assume that the surface consists

Corresponding author address: Dr. Dargan M. Frierson, Program in Applied and Computational Mathematics, Princeton University, Fine Hall, Washington Road, Princeton, NJ 08540.
E-mail: frierson@princeton.edu

of a "mixed-layer ocean," a slab of water of specified heat capacity with no horizontal transport. The model is then energetically closed, which simplifies some of our analysis, especially in Frierson et al. (2006, hereafter Part II).

We have tried to choose a boundary layer model that allows us to pass to a physically interesting dry limit as the moisture in the atmosphere is reduced to zero. The resulting dry model is very different from the sort of model described by Held and Suarez (1994), in that the atmosphere is destabilized very strongly by surface heating.

We see nothing in our formulation that prevents one from computing the solution in a nonhydrostatic model that resolves deep convection. Our hope is that the model is well-posed in the sense that the climate converges to a well-defined limit as resolution is increased to this point.

a. Static stability

An understanding of the tropospheric static stability in midlatitudes, although fundamental to any theory of the general circulation, has proven to be difficult to achieve. As in Stone (1972), many theories take the form of expressions for the horizontal component of the large-scale baroclinic eddy sensible heat flux, supplemented by the assumption that the ratio of the vertical to the horizontal components is such as to align the total flux along the dry isentropes in the free troposphere [or, as in Green (1970), at some angle between the horizontal and the isentropic slope]. The balance between the radiative destabilization and the upward sensible heat flux then determines the stability.

Held (1982) provide a slightly different framework for the study of this problem, by thinking of the tropopause height and the tropospheric static stability as being simultaneously determined by satisfying two constraints, one radiative and one dynamical. The radiative constraint between the tropospheric lapse rate and the height of the tropopause is generated by a standard radiative–convective model in which the lapse rate is an input parameter. For the dynamical constraint, Held (1982) use a theory for the depth to which unstable quasigeostrophic baroclinic eddies can penetrate into a stably stratified atmosphere in the presence of vertical shear. Thuburn and Craig (1997) perform tests of this theory using a comprehensive moist GCM, and conclude that the radiative constraint with appropriate absorber distributions is useful in explaining the relation between the tropopause height and static stability, but that the dynamical constraint in Held (1982) is not. However, Schneider (2004) shows that a related dynamical constraint does help explain the behavior of an idealized dry general circulation model. This difference in conclusions is related, at least in part, to the differences in the definition of the dynamical constraint, but potentially also to the differences in the underlying models. The work of Haynes et al. (2001) also supports the view that mixing of potential vorticity by baroclinic eddies shapes the extratropical tropopause in idealized dry models.

An alternative perspective on midlatitude static stability is that it is in fact controlled by moist convection, as in the Tropics (Emanuel 1988; Juckes 2000). The following picture is a simplified version of Juckes' argument. In earthlike conditions, midlatitude eddies typically convect up to the tropopause above the region of low-level warm, moist, poleward moving air near the surface, and have approximately neutral moist stability in this sector. Ignoring horizontal temperature gradients near the tropopause, the difference in moist static energy (MSE) between surface and tropopause in the nonconvecting regions is then given by the difference in near surface moist static energy between the warm and cold sectors of the eddy. The near-surface RMS moist static energy in midlatitude eddies is then the appropriate measure of the moist stability of these dry nonconvecting regions. Equivalently, the mean dry stability is greater than needed to maintain neutral stability given mean low-level temperature and water vapor content, but it is just sufficient to maintain neutrality given values of temperature and water vapor in the typical warm sectors of midlatitude storms. The claim is that baroclinic eddies are unable to stabilize the troposphere efficiently enough to prevent convection in the warm sectors of storms, at least for realistic strengths of radiative destabilization.

Our model provides a useful framework for testing this picture. As we vary the moisture content by orders of magnitude, we can study how the control of static stability is affected by moisture and convection. The dry limit of this model is also illuminating in diagnosing the importance of convection versus large-scale theories for static stability. There is nothing inherent to the picture described above that limits its applicability to moist atmospheres.

b. Eddy scale

In classical theory, the length scales of baroclinic eddies are thought of as determined by the most unstable mode of the standard linear baroclinic instability problems of Eady or Charney. In the Eady model, this length scale is proportional to the internal radius of deformation, $L_D = NH/f$, where N is the buoyancy frequency, H is the depth of the fluid, and f is the local value of the Coriolis parameter. In the Charney prob-

lem, the length scale depends on whether one is in the shallow eddy or deep eddy regime, the transition from the former to the latter occurring when the isentropic slope exceeds $H\beta/f$. If the deep eddy regime is the relevant one, the most unstable wavelength is once again proportional to the familiar radius of deformation, with H now proportional to the scale height. The dry static stability of the atmosphere (measured by the buoyancy frequency N) is, from this perspective, a key ingredient in any theory for eddy length scales.

An alternate theory for the length scale comes from turbulence theory. Simulations of two-dimensional turbulence develop an inverse cascade of energy to large scales, and the energy containing eddy scale is determined not by the injection scale, but by whatever factor stops the cascade. In particular, an environmental vorticity gradient can stop the cascade (Rhines 1975). In the homogeneous turbulence simulations of quasigeostrophic baroclinically unstable flows described by Held and Larichev (1996), the eddy scale is clearly determined by this process, resulting in an eddy scale that is proportional to the Rhines scale, $L_\beta = \sqrt{v_{\mathrm{RMS}}/\beta}$, where v_{RMS} is the square root of the eddy kinetic energy. Full moist GCM simulations described by Barry et al. (2002) provide some evidence that the Rhines scale is also relevant in this more realistic context, even though it is unclear whether anything resembling a well-defined inverse cascade exists in these simulations. In contrast, Schneider (2004) has argued that it is difficult to separate the radius of deformation and the Rhines scale in models in which the static stability in free to adjust [unlike the quasigeostrophic (QG) turbulence models described above]. The claim by Barry et al. (2002) that the Rhines scale fits their model results better than does the radius of deformation evidently implies that one can separate these scales in their moist GCM.

If the Rhines scale is the relevant scale, then the effect of the static stability on this scale is indirect. A decrease in static stability, for example, could increase the eddy kinetic energy and thereby increase the eddy scale. This is what occurs in the QG homogenous theory of Held and Larichev (1996), for example.

Our concern here is with the effects of latent heat release on eddy scales. Expectations based on linear theory are described by Emanuel et al. (1987), who study a moist Eady model in which regions of upward motion (updrafts) are assumed to be saturated. The condensation that occurs in the updrafts acts to reduce the stability there to an effective moist value. In the limit of moist neutrality in the updrafts, they find that the width of the updrafts collapses to zero, and that the total wavelength of the shortwave cutoff is roughly divided by two compared with the dry case. The dry static stability continues to control the scale of the unstable modes in this limit. The same result would be obtained by considering a single, averaged static stability roughly halfway between the dry and moist values relevant in the downdraft and updraft.

From a rather different perspective, Lapeyre and Held (2004) attempt to extend the results for dry baroclinic QG turbulence to the moist case. For weak latent heating, the solutions can be qualitatively understood in terms of a reduced moist static stability. However, the eddy scale in this turbulent model can increase as one increases the moisture content, since the flow can become more energetic, and, as alluded to above, the eddy scale can expand due to a more extensive inverse cascade.

We investigate the role of the static stability and moisture in the determination of eddy scales within our model by varying the moisture content of the atmosphere. A key difference with our moist GCM compared with the theoretical models mentioned above is that the static stability can adjust with the moisture content. On the one hand, we have found it difficult to relate our results to the body of work outlined above. On the other hand, the results suggest that there are strong and, we suspect, simple constraints on the midlatitude eddy scale.

c. Outline

In section 2 we give a complete description of this simplest version of the model, including the dynamical core, the boundary conditions and mixed layer ocean, the surface flux, boundary layer, and condensation schemes. Also included in this section is a table containing all of the parameters in our model. Our intent in providing this detailed description is to make this computation easily reproducible. In section 3 we present the basic climatology of both the control version of the model and the dry limit. In section 4, we present results concerning the static stability under different model configurations, including increasing the water vapor content and varying the meridional gradient of insolation. We present results concerning eddy scales in section 5, and conclude in section 6.

2. Model description

a. Boundary conditions

The lower boundary condition is an aquaplanet (ocean covered) surface with no topography. For the ocean surface, we choose an energy-conserving slab mixed layer with shallow depth rather than fixed sea

surface temperatures. The mixed layer has a specified heat capacity and single temperature which adjusts satisfying the following equation:

$$C_O \frac{\partial T_s}{\partial t} = R_S - R_{Lu} + R_{Ld} - L_v E - S \qquad (1)$$

where C_O is a specified heat capacity, T_s is the local surface temperature, L_v is the latent heat of vaporization, E is the evaporative flux, S is the sensible heat flux, and R_S, R_{Lu}, R_{Ld} are the net shortwave, upward longwave flux, and downward longwave radiative fluxes, respectively.

b. Radiation

Because we are using surface fluxes to drive the slab ocean temperatures we require upward and downward fluxes and not simply heating rates as in the Newtonian cooling scheme commonly used in idealized models. We choose gray radiative transfer with specified longwave absorber distribution as the simplest alternative. Therefore, while water vapor is a prognostic variable in this model, changes in it do not affect the radiative transfer. We regard this as a key simplification; it allows us to study some of the dynamical consequences of increasing or decreasing the water vapor content in isolation from any radiative effects. There are no clouds in this model. Radiative fluxes are a function of temperature only. We do not claim that the dynamical effects isolated in such a model dominate over radiative effects when, say, the climate is perturbed as in global warming simulations. But we do argue that it is very helpful to isolate the dynamical from the radiative effects in this way in order to build up an understanding of the fully interactive system.

We idealize solar radiation as a specified heating of the surface, a function of latitude only. No solar radiation is absorbed by the atmosphere. There is no seasonal or diurnal cycle in the model. The solar flux is

$$R_S = R_{S0}[1 + \Delta_s p_2(\theta)] \qquad (2)$$

where

$$p_2(\theta) = \frac{1}{4}[1 - 3\sin^2(\theta)] \qquad (3)$$

is the second Legendre polynomial, R_{S0} is the global mean net solar flux, and Δ_s can be varied in order to drive the system to larger or smaller meridional temperature gradients. We have excluded solar absorption in the atmosphere for simplicity, but also because of a desire to accentuate the strength of the radiative destabilization of the atmosphere, so to more clearly differentiate this model from those, such as Held and Suarez (1994), in which the radiative destabilization is very weak.

In the infrared, we specify the atmospheric optical depths as a function of latitude and pressure to approximate the effects of water vapor. The surface values are given the form

$$\tau_0 = \tau_{0e} + (\tau_{0p} - \tau_{0e})\sin^2(\theta) \qquad (4)$$

where τ_{0e} and τ_{0p} give surface values at the equator and pole, respectively. The structure with height consists of a term that is quartic in pressure and a linear term:

$$\tau = \tau_0\left[f_l\left(\frac{p}{p_s}\right) + (1 - f_l)\left(\frac{p}{p_s}\right)^4\right]. \qquad (5)$$

The quartic term approximates the structure of water vapor in the atmospheric (since water vapor–scale height is roughly ¼ of the density-scale height and optical depth is roughly logarithmic in mixing ratio). If we use this quartic term in isolation, the stratospheric radiative relaxation time becomes very long, which is both unrealistic and awkward from the perspective of reaching equilibrium within a reasonable length integration. The small linear term is included to reduce the stratospheric relaxation times. The stratosphere is clearly one of the more unrealistic aspects of this model.

The standard two-stream approximation is used to calculate the radiative fluxes. The radiative equations we integrate are

$$\frac{dU}{d\tau} = (U - B) \qquad (6)$$

$$\frac{dD}{d\tau} = (B - D), \qquad (7)$$

where U is the upward flux, D is the downward flux, and $B = \sigma T^4$. The diffusivity factor that commonly appears multiplying the rhs of these equations has been folded into the optical depth. The boundary condition at the surface is $U[\tau(z = 0)] = \sigma T_s^4$ and at the top of the atmosphere is $D(\tau = 0) = 0$. The radiative source term in the temperature equation is

$$Q_R = -\frac{1}{c_p \rho}\frac{\partial(U - D)}{\partial z}. \qquad (8)$$

Our choice of a parameter set for our control integration is listed, along with those for the other parameterization schemes, in Table 1.

c. Surface fluxes

We utilize standard drag laws, with drag coefficients that are equal for momentum, temperature, and water.

TABLE 1. Complete parameter list. The parameters that we vary in this study are e_0^* and Δ_s.

Parameter	Explanation	Control value
	Numerics and dynamics parameters	
ν	Hyperdiffusion coefficient	10^{16} m^4 s^{-1}
r	Robert coefficient	0.03
Ω	Earth rotation rate	7.292×10^{-5} s^{-1}
g	Gravitational acceleration	9.8 m s^{-2}
a	Earth radius	6.376×10^6 m
c_p	Specific heat of dry air	1004.64 J kg^{-1} K^{-1}
R_d	Gas constant for dry air	287.04 J kg^{-1} K^{-1}
p_{s0}	Mean atmospheric surface pressure	10^5 Pa
	Boundary condition parameters	
C_O	Oceanic mixed layer heat capacity	10^7 J K^{-1} m^{-2}
	MOS parameters	
κ	von Kármán constant	0.4
z_0	Roughness length	3.21×10^{-5} m
Ri_c	Critical Richardson number for stable mixing cutoff	1
	Boundary layer parameters	
f_b	Surface layer fraction	0.1
	Radiation parameters	
R_{S0}	Net solar constant (includes albedo)	938.4 W m^{-2}
Δ_s	Latitudinal variation of shortwave radiation	1.4
τ_{0e}	Longwave optical depth at the equator	6
τ_{0p}	Longwave optical depth at the pole	1.5
f_l	Linear optical depth parameter (for stratosphere)	0.1
σ	Stefan–Boltzmann constant	5.6734×10^{-8} W m^{-2} K^{-4}
	Humidity and large-scale condensation parameters	
L_v	Latent heat of vaporization of water	2.5×10^6 J kg^{-1}
R_v	Gas constant for water vapor	461.5 J kg^{-1} K^{-1}
e_0^*	Saturation vapor pressure at 273.16 K	610.78 Pa

For the surface stress, sensible heat flux, and evaporation, respectively, we have

$$\mathcal{T} = \rho_a C |\mathbf{v}_a| \mathbf{v}_a \tag{9}$$

$$S = \rho_a c_p C |\mathbf{v}_a| (\Theta_a - \Theta_s) \tag{10}$$

$$E = \rho_a C |\mathbf{v}_a| (q_a - q_s^*), \tag{11}$$

where c_p is the heat capacity at constant pressure, Θ_s is the surface potential temperature and q_s^* is the saturation specific humidity at the surface temperature, while $\mathbf{v}_a$, ρ_a, Θ_a, and q_a are the horizontal wind, density, potential temperature, and specific humidity evaluated at the lowest model level.

The drag coefficient, calculated according to a simplified Monin–Obukhov similarity (MOS) theory, is specified as

$$C = \kappa^2 \left(\ln \frac{z_a}{z_0} \right)^{-2} \quad \text{for} \quad \mathrm{Ri}_a < 0 \tag{12}$$

$$C = \kappa^2 \left(\ln \frac{z_a}{z_0} \right)^{-2} (1 - \mathrm{Ri}_a/\mathrm{Ri}_c)^2 \quad \text{for} \quad 0 < \mathrm{Ri}_a < \mathrm{Ri}_c \tag{13}$$

$$C = 0 \quad \text{for} \quad \mathrm{Ri}_a > \mathrm{Ri}_c, \tag{14}$$

where κ is the von Kármán constant, z_a is the height of the lowest model level, z_0 is the surface roughness length, Ri_a is the bulk Richardson's number evaluated at the lowest model level, and Ri_c is a value of Ri_a above which there is no drag. The bulk Richardson's number at the lowest model level is defined as

$$\mathrm{Ri}_a = \frac{gz[\Theta_v(z_a) - \Theta_v(0)]/\Theta_v(0)}{|v(z_a)|^2}, \tag{15}$$

with g the gravitational acceleration and Θ_v is the virtual potential temperature. In our model we replace Θ_v by the virtual dry static energy, $c_p T_v + gz$, with T_v the virtual temperature. The expressions (12)–(14) are consistent with Monin–Obukhov similarity theory, with the unstable case treated as neutral (i.e., with the universal stability function $\Phi = 1$), and the stable case with universal stability function $\Phi = 1 + \mathrm{Ri}_c^{-1}\zeta$, where ζ is the vertical coordinate scaled by the Monin–Obukhov length. If the surface is unstable, the drag coefficient is independent of the Richardson number. If the surface is stable, the drag coefficient is reduced with increased surface stability, approaching zero as Ri_a approaches Ri_c.

Our standard value for the surface roughness length ($z_0 = 3.21 \times 10^{-5}$ m) gives a drag coefficient $C = 0.001$ when the winds are specified at $z = 10$ m in unstable or neutral situations. We use zero gustiness velocity in this model, so that the surface fluxes are allowed to approach zero over small surface winds. As a note of caution, we have observed the tropical precipitation distributions to be sensitive to the formulation of the unstable side of the surface flux formulation.

d. Boundary layer

The boundary layer depth h is set to the height where another bulk Richardson number

$$\mathrm{Ri}(z) = \frac{gz[\Theta_v(z) - \Theta_v(z_a)]/\Theta_v(z_a)}{|v(z)|^2} \tag{16}$$

exceeds Ri_c. Diffusion coefficients within the boundary layer are calculated in accordance with the simplified Monin–Obukhov theory used for the drag coefficient. Fluxes are matched to a constant-flux surface layer, which is assumed to occupy a specified fraction f_b of the boundary layer depth, and go to zero at the top of the boundary layer, with the following functional forms for diffusivity (Troen and Mahrt 1986):

$$K(z) = K_b(z) \quad \text{for} \quad z < f_b h \tag{17}$$

$$K(z) = K_b(f_b h)\frac{z}{f_b h}\left[1 - \frac{z - f_b h}{(1 - f_b)h}\right]^2 \quad \text{for} \quad f_b h < z < h, \tag{18}$$

with the surface layer diffusion coefficients K_b chosen to be consistent with the simplified Monin–Obukhov theory; that is,

$$K_b(z) = \kappa u_a \sqrt{C} z \quad \text{for} \quad \mathrm{Ri}_a < 0 \tag{19}$$

$$K_b(z) = \kappa u_a \sqrt{C} z\left[1 + \frac{\mathrm{Ri}}{\mathrm{Ri}_c}\frac{\ln z/z_0}{(1 - \mathrm{Ri}/\mathrm{Ri}_c)}\right]^{-1} \quad \text{for} \quad \mathrm{Ri}_a > 0, \tag{20}$$

where the subscript a again denotes the quantity evaluated at the lowest model level, and C is the drag coefficient calculated from Eqs. (12)–(14). These diffusion coefficients are used for momentum, dry static energy, and specific humidity.

The model in its dry limit is sensitive to Ri_c. Increasing the value of Ri_c allows more penetrative convection, modifying boundary layer depths and dry static energy profiles. However, a study of the effects of different choices of this parameter on our results has shown the qualitative results to be robust.

e. Large-scale condensation

While we have constructed versions of this model with convection schemes, the model can also be run with large-scale condensation only. As another example of a general circulation model run without a convection scheme, see Donner et al. (1982) and Donner (1986). Humidity and temperature are only adjusted when there is large-scale saturation of a gridbox; that is, when $q > q^*$. As is standard, the adjustment is performed implicitly using the derivative dq^*/dT, so that latent heat released during condensation does not cause the gridbox to become undersaturated:

$$\delta q = \frac{q^* - q}{1 + \dfrac{L_v}{c_p}\dfrac{dq^*}{dT}}, \tag{21}$$

where δq is the adjustment to the specific humidity q, q^* is the saturation specific humidity, and L_v is the latent heat of vaporization. The precipitation falls out immediately, but is reevaporated below. We use the rather extreme assumption that each layer below the level of condensation must be saturated by reevaporation for the rain to fall below this level, so the column must be saturated all the way down for precipitation to reach the ground. Reevaporation is yet another potentially significant factor in this model.

We use an expression for the saturation vapor pressure e^* that follows from the Clausius–Clapeyron equation assuming fixed latent heat of vaporization L_v:

$$e^*(T) = e_0^* e^{-(L_v/R_v)[(1/T) - (1/T_0)]}, \tag{22}$$

with the constant e_0^* (the saturation vapor pressure at $T_0 = 273.16$ K) left as our key model parameter that we vary in order to change the humidity content of the atmosphere. The saturation specific humidity is calculated from $q^* = \varepsilon e^*/p$ where $\varepsilon = R_d/R_v$ and p = pressure. No freezing is considered in the model. An alternative method to changing the importance of moisture is by varying the latent heat of vaporization L_v in all equations except the Clausius–Clapeyron relation. This is equivalent to varying the e_0^* parameter except for the virtual temperature effect, as the atmospheric moisture content is different with these two methods.

The resulting model is sensitive to horizontal resolution in the Tropics, more so than a prototype model with convective parameterization that we have also analyzed (Frierson 2006, manuscript submitted to *J. Atmos. Sci.*), but midlatitudes are quite insensitive both to resolution (as described below) and to inclusion of a convection scheme. Since we are focusing on midlatitudes in this study, we have chosen to utilize this simplest of models to avoid the additional complexity introduced by the convective parameterization. We

hope that this description of our model's column physics package is complete enough to allow others to replicate our results.

f. Dynamical core

To integrate the primitive equations, we run with a standard Eulerian spectral dynamical core with triangular truncation, using leapfrog time integration with Robert filter, and fourth-order hyperdiffusion. In this study, we run with resolutions varying up to T170 (corresponding to 0.7° horizontal resolution).

We use sigma coordinates, with 25 levels spaced according to the expression $\sigma_c = \exp[-5(0.05\tilde{z} + 0.95\tilde{z}^3)]$ where $\tilde{z}$ is equally spaced in the unit interval. This provides additional resolution in the stratosphere and boundary layer. We use a piecewise parabolic method (Collela and Woodward 1984) for vertical advection of water vapor, and a piecewise linear scheme for horizontal advection of vapor. We use the virtual temperature, which accounts for the density of water vapor, when calculating the geopotential, but we have ignored the difference between the heat capacities of water vapor and dry air. We also ignore the fact that the mass of the atmosphere should be changed by precipitation.

Energy and moisture are both corrected by a multiplicative factor to ensure exact conservation by dynamics. Because of the nature of the numerical method and typical profiles of velocity and humidity, the moisture correction produces a systematic sink of water vapor, the strength of which is a function of resolution (with less correction necessary at higher resolution). At low resolutions, this causes the stratospheric water vapor to be constrained very close to zero. Since water vapor does not feed back into our radiation calculation, this has little effect on the troposphere of our model, with the exception of small relative humidity differences in the upper troposphere.

3. Basic climatology

Integrations have been performed with $e_0^* = \xi e_0^*$(control), with $\xi = 0.0, 0.5, 1.0, 2.0, 4.0$, and 10.0, and with e_0^*(control) = 610.78 Pa. All experiments have been integrated at T85 resolution, with $\xi = 0$, 1, and 10 also integrated at T170. Each of these is run for 1080 days. The simulations start with uniform temperature, and the first 360 days are discarded as spin up. The last 720 days are used for averaging. All time mean quantities are calculated from averages over each time step of the model, whereas spectra are calculated using instantaneous values, sampled once per day. The experiments with $\xi = 10$ are referred to as 10X, etc., the case with $\xi = 0$ as the dry limit, and the case with $\xi = 1$ as the control in the following. The simulations and plots we describe are at T170 resolution unless otherwise noted.

Snapshots of the precipitation distribution for the control run at T170 and at T85 resolution are given in Fig. 1. The primary effect of not having a convection scheme is the presence of small scale storms (often 3–4 grid points in size) exploding throughout the Tropics. Some of these storms propagate into the subtropics and take on some features expected of tropical storms. In midlatitudes, by contrast, the precipitation is characterized by baroclinic wavelike structures.

To examine convergence with resolution in midlatitudes, we plot the zonal mean surface winds and the vertically averaged spectrum for the meridional velocity (discussed in detail in section 5) for T42, T85, and T170 for the control run in Fig. 2. In these fields, T42 departs significantly from T85 and T170; the maximum surface winds are weaker and shifted equatorward, and the spectrum displays a less peaked maximum. The T42 case has slightly smaller eddy length scale than the higher resolution cases.

Figure 3a shows the zonally averaged zonal winds as a function of pressure in the control case. The maximum zonal wind of 30.0 m s^{-1} occurs at (42.5°, 217 hPa), the maximum surface winds of 9.7 m s^{-1} at 47°, and the strongest easterlies at (11°, 900 hPa), with magnitude -9.8 m s^{-1}. There is evidence of separation of the Hadley cell, or subtropical, jet with maximum near 25°, and an eddy-driven jet, with maximum near 45°.

Virtual dry static energy (divided by c_p) is shown in Fig. 4a. There is a 53 K equator-to-pole virtual temperature difference at the lowest model level. Midlatitudes are statically stable for dry disturbances, with $\partial\Theta_v/\partial z = 4.1$ K km^{-1} averaged from 30° to 60° between the surface and the tropopause. On the same figure, we plot the tropopause based on the World Meteorological Organization (WMO) definition: the lowest level where the lapse rate reaches (and stays above) 2 K km^{-1}. The tropical and extratropical tropopauses are clearly distinguished. The tropopause height is found to be relatively insensitive to the lapse rate criterion, except in polar regions. The moist stability of the model is described in section 4.

The standard Eulerian meridional overturning streamfunction is plotted in Fig. 5a (note the different contour intervals for direct and indirect circulations). There is a very strong Hadley cell, with maximum strength of 260 Sv = 2.6×10^{11} kg s^{-1} [we use the Sverdrup (Sv) here as a unit of mass transport instead of the typical water volume transport]. This is approximately 3 times the observed annual mean strength. The Ferrel cell, with a maximum strength of 54 Sv at 40°, is

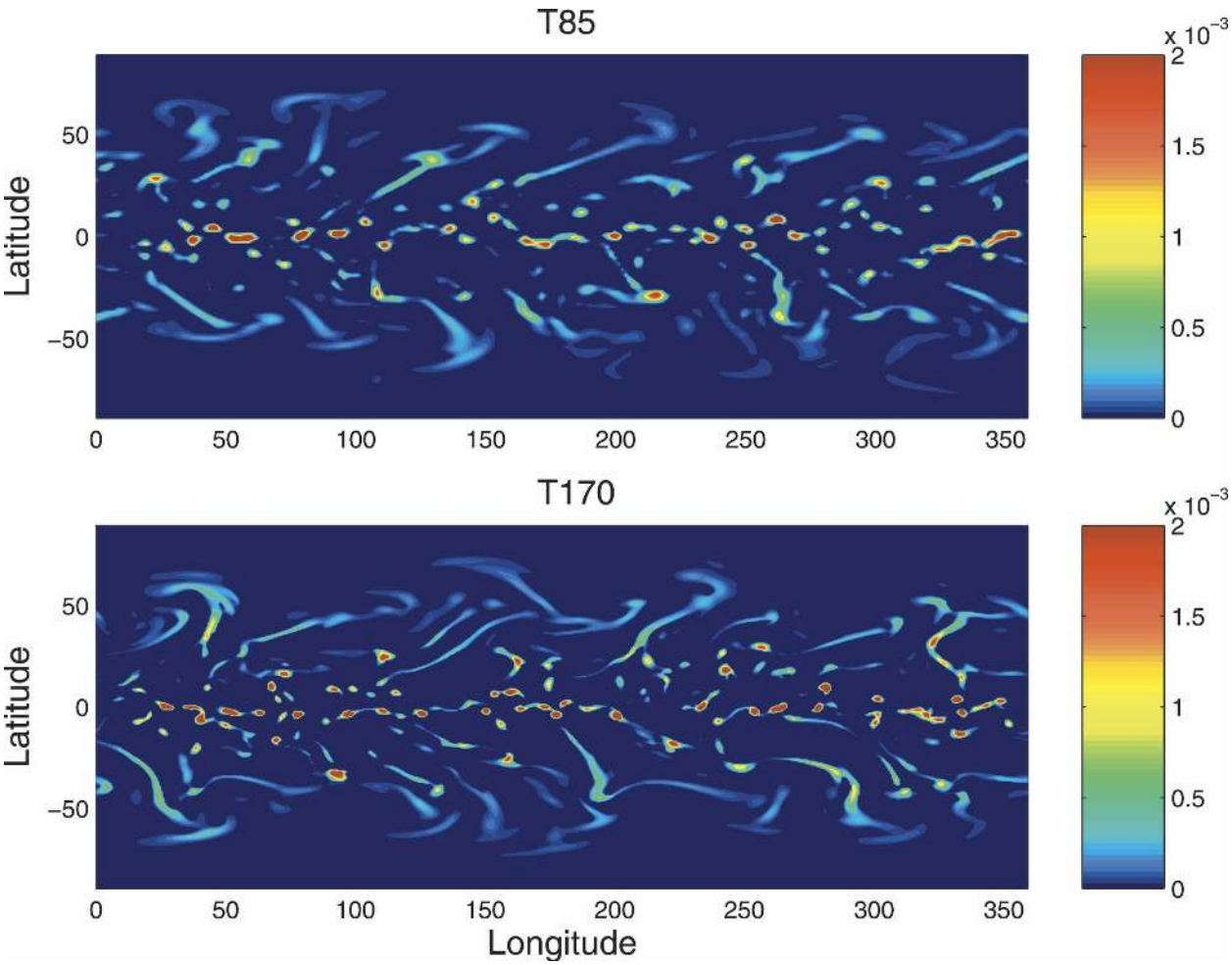

FIG. 1. Instantaneous precipitation distributions (kg m^{-2} s^{-1}) for the control case at T85 resolution and at T170 resolution.

comparable to that in annual mean observations. The Hadley cell strength is somewhat sensitive to model resolution (285 Sv at T85, 265 Sv at T42).

There are at least three aspects of our model formulation that conspire to create a very strong Hadley cell: absence of oceanic heat transport, absence of a convective parameterization scheme, and absence of absorption of solar radiation within the atmosphere. In experi-

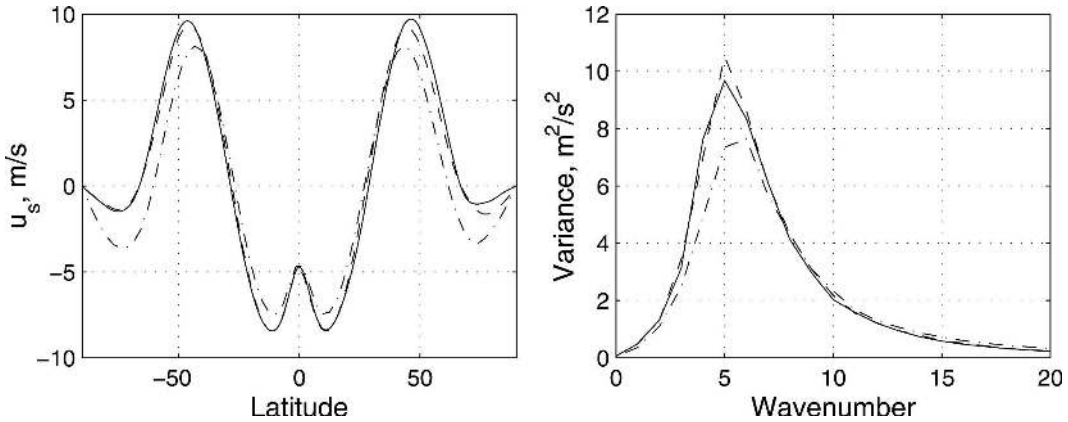

FIG. 2. (left) Resolution dependence of time mean zonal mean surface zonal winds. (right) Resolution dependence of zonal wavenumber spectra for $\langle v \rangle$ at 45° latitude. T170 (solid), T85 (dashed), and T42 (dash-dot).

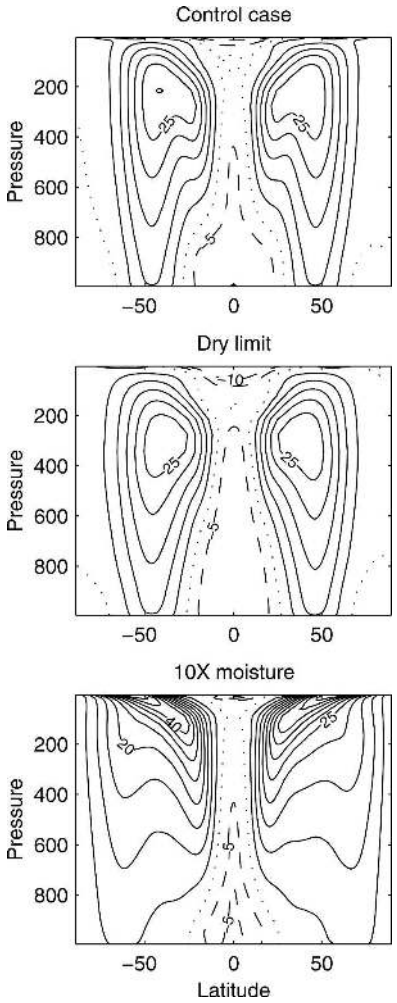

FIG. 3. Time mean zonal mean zonal winds ($m\,s^{-1}$) for the control case, the dry limit, and the 10X case. The contour interval is 5 $m\,s^{-1}$ and the zero contour is shown with dotted lines.

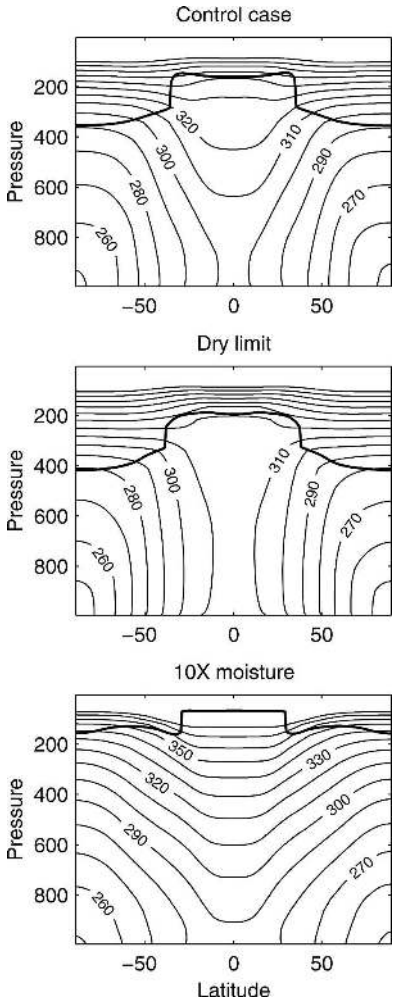

FIG. 4. Time mean zonal mean virtual dry static energy (K) for the control case, the dry limit, and the 10X case. The contour interval is 10 K. The WMO tropopause is shown with the bold line.

ments in which we include the latter two effects, the Hadley cell is reduced to the still large value of 175 Sv.

Finally, the relative humidity distribution is plotted in Fig. 6a. The deep Tropics are close to saturation everywhere. The local minimum in the subtropical subsidence regions is 43%, significantly larger than observations, despite the strength of the overturning. In the polar regions, the relative humidity is quite high, above 70% relative humidity for almost the entire troposphere from 55° poleward.

Returning to Figs. 3–6, we have also plotted the corresponding figures for the dry and 10X simulations. The similarity of the zonal mean winds (Fig. 3) in the dry and control cases is remarkable. The hint of a two jet structure present in the control is absent in the dry limit, however. In the 10X model in contrast, the surface winds have shifted poleward substantially and have weakened. We plot in Fig. 7 the profiles of upper-tropospheric winds for all values of ξ examined. The poleward shift and weakening occur gradually as ξ increases beyond unity. There is only a slight hint of equatorward movement and strengthening when we reduce the moisture content of the atmosphere below that in the control. The upper-tropospheric winds in the Tropics and subtropics change little with moisture content, despite, as we will see, a large change in the Hadley circulation.

Figure 4 shows a significant change in dry static stability with moisture content. This is true in the Tropics, where temperatures follow the moist adiabat, but also in the extratropics, which we discuss in more detail in section 4. In the dry limit, the isentropes are essentially vertical in the Tropics, and surprisingly near vertical for a large part of the rest of the troposphere. The polar

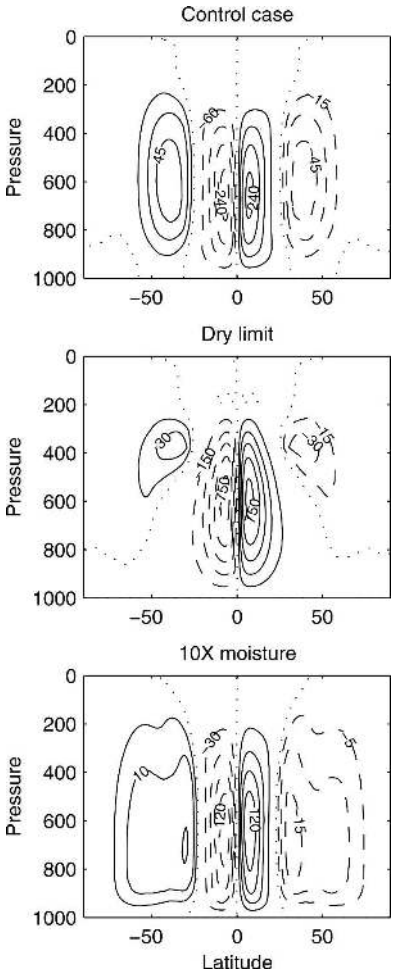

FIG. 5. Time mean zonal mean streamfunction (10^9 kg s^{-1}) for the control case, the dry limit, and the 10X case. Note the different contour intervals for direct and indirect circulations for each plot. The contour intervals for (direct, indirect) circulations are (60, 15) for the control case, (150, 15) for the dry limit, and (30, 5) for the 10X case (all expressed in 10^9 kg s^{-1}).

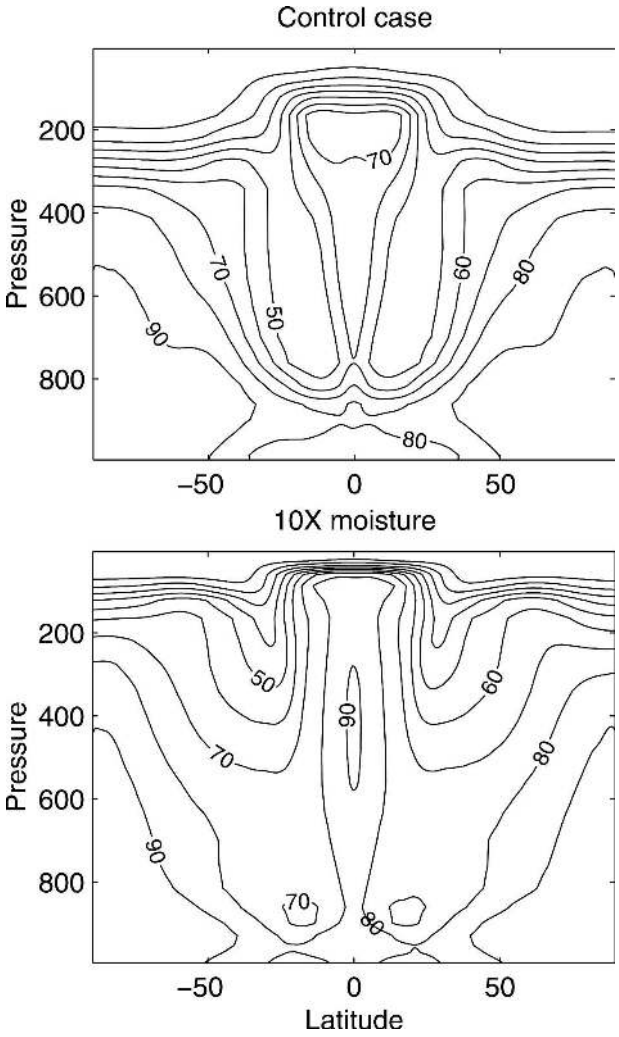

FIG. 6. Time mean zonal mean relative humidity (%) for the control case and the 10X case. The contour interval is 10%.

regions remain stable for all cases. Again we overlay the tropopause height, calculated from the WMO criterion: the tropopause is slightly lower than in the control case everywhere for the dry limit, and significantly higher everywhere in the 10X case. In the dry limit the average vertical gradient of potential temperature below the tropopause from 30° to 60° is $\partial\Theta_v/\partial z$ = 2.2 K km^{-1} with most of this stability contributed by the layer just beneath the tropopause; the corresponding average stability for the 10X case is $\partial\Theta_v/\partial z$ = 6.5 K km^{-1}.

Figure 8 summarizes the pole-to-equator temperature and moist static energy differences at the lowest model level as a function of ξ for all cases. There is a gradual decrease of the temperature gradient and increase of the moist static energy gradient as ξ is increased. Most of these changes in this figure result from changes at the equator, where temperatures decrease and moist static energy increases with moisture content. Polar temperatures are approximately fixed in all cases. We discuss factors controlling the low level moist static energy gradient in Part II.

Examining the streamfunction (Figs. 5b,c; note the different contour intervals for direct and indirect circulations, and for each plot), we see the presence of a much stronger Hadley cell in the dry case, extending further poleward as well. The strength of the overturning is 810 Sv, exceeding the value in the control case by a factor of 3. This corresponds to meridional winds of nearly 8 m s^{-1} in the time mean in both the upper and lower troposphere. In this case, a direct circulation exists for all latitudes within the boundary layer. A small region of indirect circulation remains, but only in the

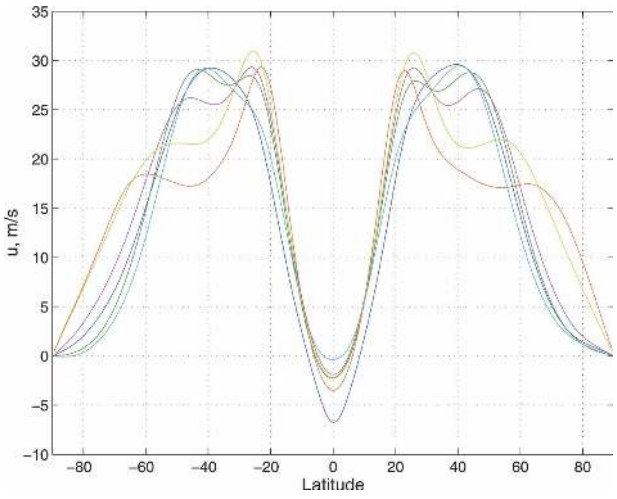

FIG. 7. Zonal winds at 276 mb for the dry limit (blue), the control case (green), and the 10X case (red) at T170 resolution, and 0.5X case (cyan), 2X case (magenta), and 4X case (yellow) at T85 resolution.

midlatitude upper troposphere. This Ferrel cell, weakened to 40 Sv, cannot penetrate into the area dominated by boundary layer mixing, where diffusive momentum fluxes dominate over the large-scale eddy fluxes. Poleward energy transport in the Tropics is similar in the two models despite the very different Hadley cell strengths (see Part II). The Hadley cell in the 10X case is weakened to 145 Sv, but we caution the reader that this value is sensitive to resolution. Additionally the Ferrel cell is much weaker (12 Sv), is displaced poleward, and shows evidence of splitting into two cells.

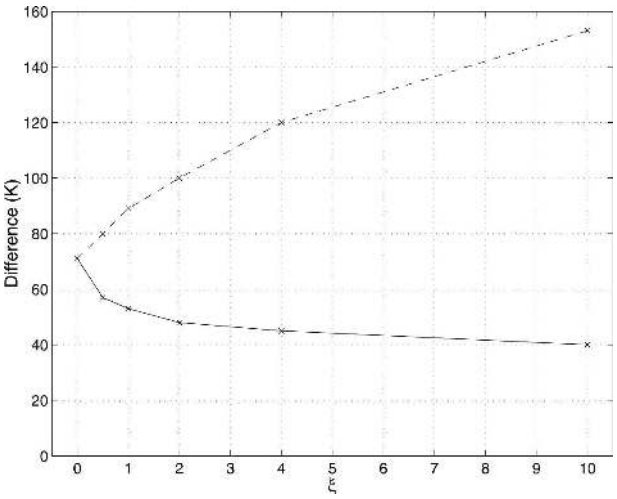

FIG. 8. Equator-to-pole virtual temperature difference at the lowest model level (solid), and moist static energy difference at the lowest model level (dashed) for all humidity cases.

The relative humidity for the 10X case is plotted in Fig. 6b. With the exception of the area just above the boundary layer and part of the midlatitude free troposphere, the 10X case has higher relative humidity than the control case. In particular, the subtropics and tropical regions are both significantly closer to saturation; the 10X case exceeds the control case by 33% RH at the location of minimum relative humidity in the subtropics.

The simulations show increasing separation between the subtropical and eddy-driven jets as the atmosphere is moistened. These two jets are merged in the dry run, show a hint of separation in the control, and separate for larger values of ξ. As moisture is increased the subtropical jet tightens and the eddy-driven jet moves poleward. This is listed in Table 2, which gives the location of the maximum surface westerlies as a function of ξ. Figure 9 shows the vertically integrated eddy kinetic energy (EKE) as a function of latitude for different values of ξ. Not surprisingly, the eddies also move poleward with the jet.

The poleward shift in this model can be explained, we believe, in terms of the preferential stabilization of baroclinic eddies at low latitudes. As moisture is added, the meridional temperature gradient decreases and the static stability increases, both effects leading to a flattening of the (dry) isentropic slope, which we believe is related to the reduction in EKE. The reduction in global-mean EKE is apparent in Fig. 9; however, it is also apparent in that figure that this stabilization occurs primarily equatorward of the jet maxima. There are at least two reasons for this. First, the meridional temperature gradient is weakened the most at low latitudes (where moisture represents a larger fraction of the moist static energy). Additionally, the stabilizing effect of β is strongest at low latitudes, so these latitudes are stabilized most strongly when the isentropic slope is reduced (for instance, using the two-layer stability criterion, the critical isentropic slope increases equatorward with $\beta H/f$). In the experiments with $\xi < 1$, it appears that the eddy-driven jet cannot move further equatorward, as it encounters the very weak tempera-

TABLE 2. Latitudinal position of maximum surface westerlies as a function of moisture content ξ.

ξ	Latitude
0	46.0
0.5	44.1
1.0	46.7
2.0	49.7
4.0	56.7
10.0	64.9

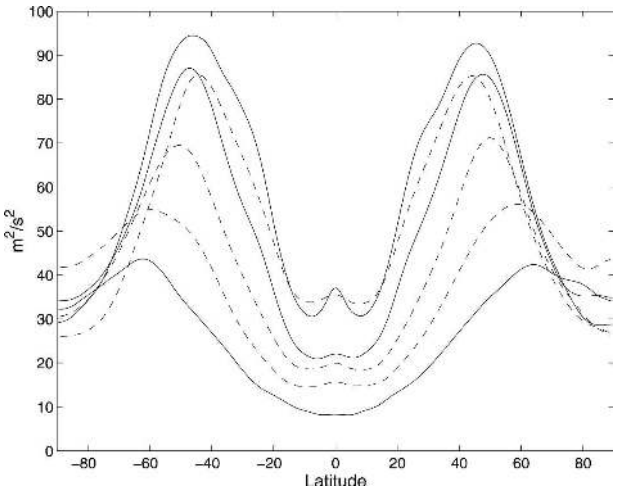

FIG. 9. Eddy kinetic energy, averaged over pressure, for the control case, the dry limit, and the 10X case at T170 (solid lines, maxima decrease with moisture), and the 0.5X case, 2X case, and 4X case at T85 (dashed lines, maxima decrease with moisture).

ture gradients maintained by the Hadley cell. At this point it is unclear whether the increase in static stability is important for the jet movement, or whether the shift can be explained simply by the reduction in temperature gradients.

4. Static stability

a. Dry limit

We first examine the static stability in the dry limit. In this case the convection is simply boundary layer diffusion, which has a well-defined top, the boundary layer depth. As seen in an instantaneous plot of boundary layer depth (Fig. 10a), depths approaching the tropopause height are observed out to midlatitudes. We plot the probability density function of the planetary boundary layer depth on top of the time-mean dry static energy in Fig. 10b. In the Tropics there is almost always dry convection to the tropopause. In midlatitudes, there is naturally little mean stratification in the lower troposphere, in regions where the boundary layer is almost always present, but there is some mean stratification in the upper troposphere, where the convective mixing penetrates more sporadically. The boundary layer extends to the tropopause on occasion. This is true for all latitudes equatorward of 60°. In high latitudes, the radiative equilibrium is more stable, and the static stability is determined by a balance between radiation and the large-scale eddy fluxes. There, as in the control run, the isentropes are quasi horizontal, and convection does not reach to the tropopause as conventionally defined (but the tropopause is less well-defined at these latitudes).

The picture that emerges seems consistent with the argument of Juckes (2000), with the tropopause supported by the deepest convection in the favorable sectors of extratropical eddies. We have made an initial attempt to vary the importance of the large-scale eddies by varying the parameter Δ_s which controls the meridional variation of the solar heating, thereby modifying baroclinicity and eddy amplitudes. In addition to the control case (1.4), we have analyzed cases with both decreased (1.0) and increased (1.8) insolation gradients, at T85 resolution. (We find that the dry model is very well converged at this resolution.) We cannot increase the insolation gradient further, given our functional form, without creating negative solar heating at the poles. Eddy kinetic energy increases by 15% in the increased solar gradient case, and decreases by 16% in the reduced gradient integration. Since these changes are relatively small, we do not expect changes in the dominant balances, but we can check for consistency with expectations based on a picture of convection-dominated static stabilities.

The dry static energy and the probability density function (PDF) of the boundary layer depth remain qualitatively unchanged in these integrations. The case with increased insolation gradient is slightly more stable; however convection still extends to the tropopause equatorward of 60°, even though the temperature contrast has been increased to 88 *K* at the lowest model level. We plot the PDFs at 45° for the standard dry limit, and for $\Delta_s = 1.8$ and 1.0 in Fig. 11a. The variance of the boundary layer depth increases with increased solar gradient. As anticipated from Juckes (2000), increased variance in the depth of convection corresponds to increased stability.

We plot the difference between the dry static energy and the dry static energy at the lowest model level at 45° for these three dry cases in Fig. 11b. Increasing the solar gradient increases the bulk stability (tropopause minus surface dry stability) at this latitude from 1.4 to 1.7 to 2.1 K km^{-1} in the three cases. This bulk stability increases at all latitudes.

Juckes relates the stability to the standard deviation of the surface static energy. The values of this quantity at 45° are 4.8, 5.7, and 6.5 K for $\Delta_s = 1.0$, 1.4, 1.8. We indicate 2 times this standard deviation by vertical lines in Fig. 11b. Although it is difficult to make a precise comparison due to the arbitrariness of the determination of the tropopause, we note that these values are similar in both magnitude and relative changes to the upper-tropospheric bulk stabilities.

To create a transition to a large-eddy-dominated

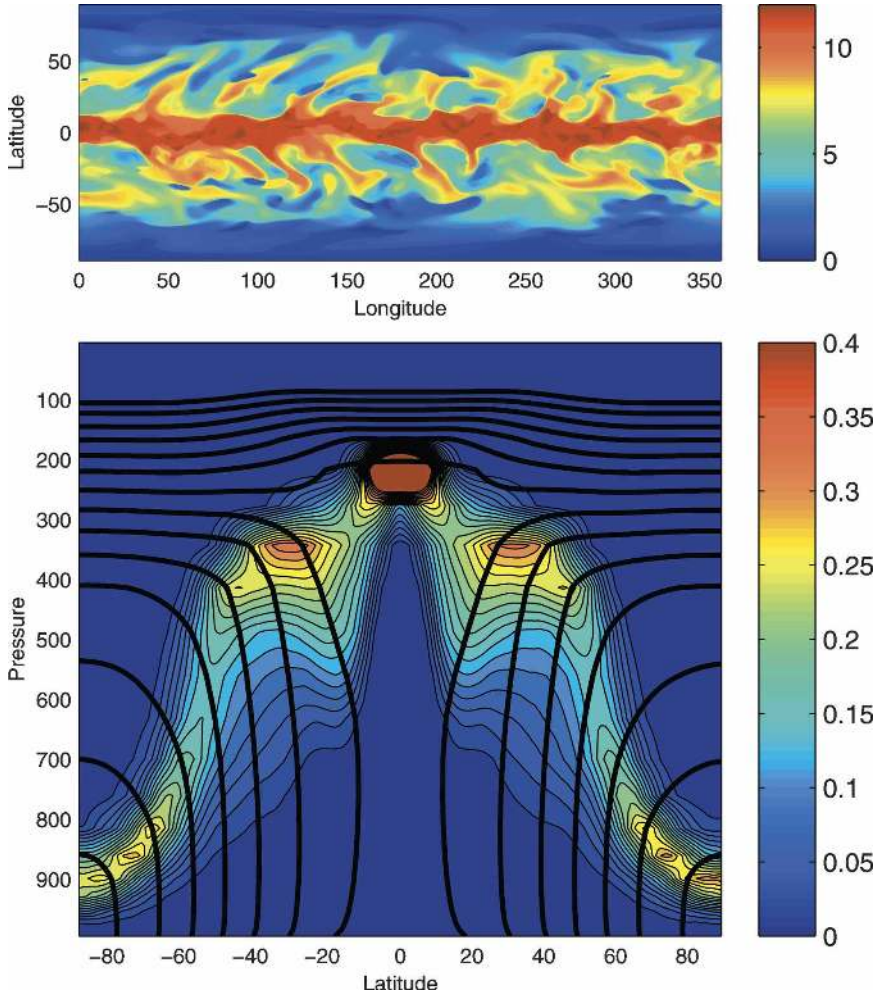

FIG. 10. (top) Instantaneous planetary boundary layer depth (in km) for the dry limit. (bottom) Probability density function of boundary layer depth at each latitude (shading) and dry static energy (contours) for the dry limit. Contour interval for DSE is 10 K.

midlatitude thermal structure, it appears that we would need to increase the strength of the eddies, or decrease the intensity of convection by dramatically reducing the radiative destabilization of the atmosphere. We have not obtained a clear transition of this sort to date. It is important to do so to make contact with dry simulations such as that of Schneider (2004). We also note that this qualitative behavior, in which stability increases as the horizontal temperature gradients increase, is also predicted by baroclinic adjustment theories (Held 1982; Schneider 2004), in which the isentropic slope is constrained to remain approximately unchanged.

b. Moist cases

There is no simple diagnostic similar to the boundary layer depth for the moist cases. We examine a bulk moist stability similar to the bulk dry stability presented in the previous section, using the difference between the saturated moist static energy and the moist static energy at the surface. These are plotted for the control case, 10X case, and dry limit in Fig. 12a–c. All three simulations are seen to be rather similar in bulk moist stability, and the level of zero buoyancy is very similar for the three cases. The large amount of conditional instability in the deep Tropics is decreased greatly when we utilize a convection scheme; poleward of this the stabilities remain similar. Above the unstable region, the 10X case is the most stable, while the dry limit is the least stable. This increased moist stability with increasing moisture can be seen in Fig. 13, where we can see that the bulk stability at the tropopause, the midtropospheric moist stability, and the amount of convective available potential energy (CAPE) all increase as moisture is added.

To explain this increased moist stability, we examine the surface standard deviation of the moist static en-

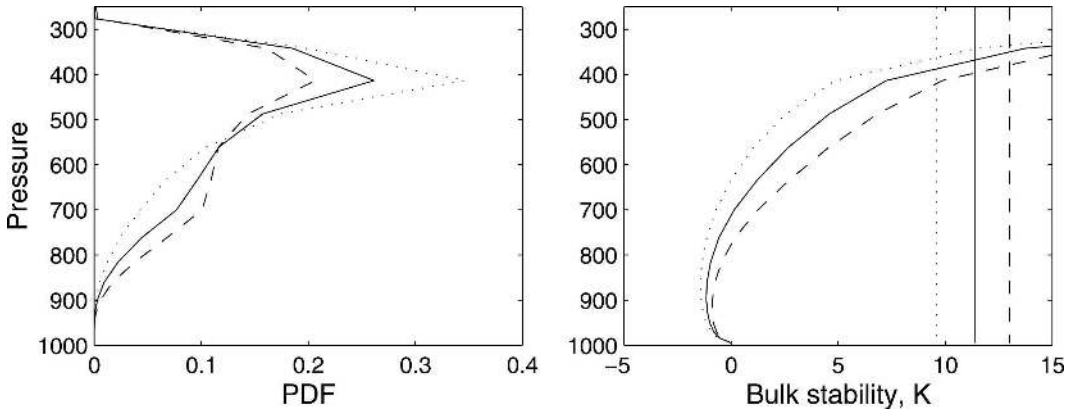

FIG. 11. (left) Probability density function of boundary layer depth at 45° latitude. (right) Dry static energy minus its surface value at 45° latitude. The vertical lines indicate twice the standard deviation of surface moist static energy; $\Delta_s = 1.4$ (default value, solid), 1.8 (dashed), and 1.0 (dotted), all dry simulations.

ergy. At 45°, these are 5.8, 7.6, and 13.5 K, for the dry limit, control case, and 10X case, respectively. Again we plot twice these standard deviations as vertical lines in Fig. 13. The precise comparison depends on the definition of the tropopause once again. Using the WMO tropopause, the bulk moist stability at the tropopause is approximately 2–2.25 times the surface MSE standard deviation for each case. We can relate the standard deviation of surface moist static energy to the gradient of this quantity at the surface, setting

$$|m'| \sim L \frac{\partial m}{\partial y}, \tag{23}$$

where L is a mixing length. The equator-to-pole moist static energy gradient increases by 25% from the dry limit to the control case, and 72% from the control case to 10X case, suggesting that to first order, the increase in the moist static energy standard deviation (by 28% and 73%) can be understood as due to the increased surface gradient with fixed mixing length. We further discuss length scales in section 5, and low-level moist static energy gradients in Part II.

Stability quantities for the National Centers for Environmental Prediction–National Center for Atmospheric Research (NCEP–NCAR) reanalysis data averaged zonally and between 2000 and 2004 are presented in Figs. 12d and 13. Especially in the Southern Hemisphere, the atmosphere has a neutrality to moist convection similar to the control case. The Southern Hemisphere, being more ocean-covered, provides a somewhat closer analog to the aquaplanet model than does the Northern. A notable difference is the lack of CAPE away from the deep Tropics in observations. Additionally, the Southern Hemisphere is a bit more strongly stratified than our model, so that a proportionality constant of 3–4 between the bulk stability and surface moist static energy standard deviation works better than the value provided above. Nevertheless, the fact remains that, as in our model, the moist stability is remarkably small over a large fraction of the tropospheric depth.

The tropopause height increases with increasing water vapor in these simulations; it is twice as high in the 10X case as in the control, in particular. These variations can be explained in terms of the radiative constraint between tropopause height and lapse rate, or equivalently a radiative–convective equilibrium model with a moist convective adjustment (as in Thuburn and Craig 1997). The decreased lapse rates in the cases with more moisture require convection to penetrate more deeply before matching smoothly onto the radiative equilibrium temperatures in the stratosphere.

5. Eddy length scales

We estimate characteristic eddy length scales using the pressure averaged wavenumber spectrum of the meridional velocity. Figure 2b gives an idea of the typical change in this quantity with resolution at 45° for the control case. The primary differences are seen in the 10X case (not shown), where scales become larger with increased resolution. In Fig. 14a, we plot the spectrum of this quantity at 45° as the moisture content of the model is varied. It is clear from this figure that the typical scales of eddies change remarkably little as we vary the moisture content. The wavenumber of maximum variance is at wavenumber 5 for all cases but the 0.5X case, which has a maximum at wavenumber 6. Further, the spectral shape is nearly unchanged. A

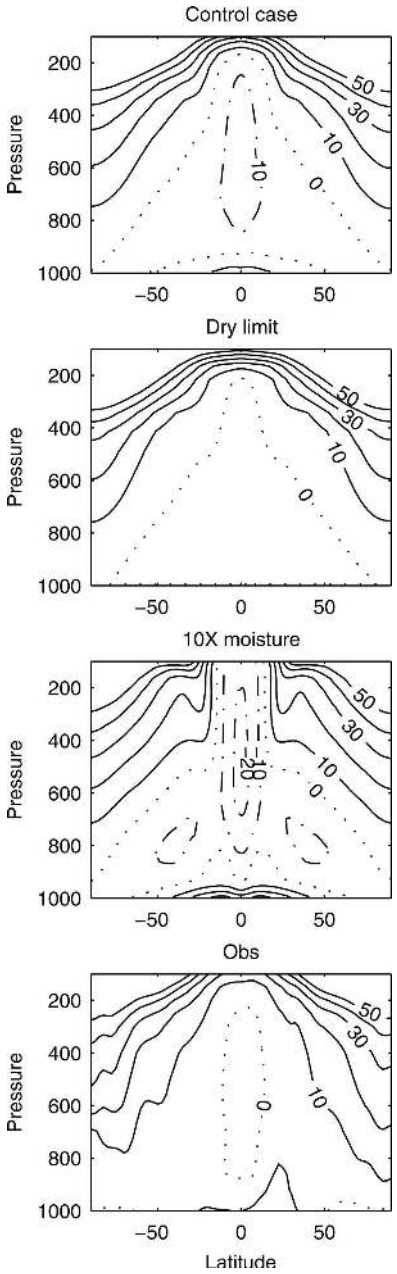

FIG. 12. Bulk moist stabilities, defined as saturated MSE minus MSE at the surface for the control case, the dry limit, the 10X case, and the NCEP–NCAR reanalysis data, 2000–04. Contour interval is 10 K.

closer look shows that the 10X case has a slightly flatter spectrum, with more fractional variance at lower wavenumbers and at higher wavenumbers than the other cases, but we do not see this clearly in the intermediate moisture cases. There is little support here for the idea that increased moisture preferentially strengthens smaller-scale storms.

For better comparison with various theories for the

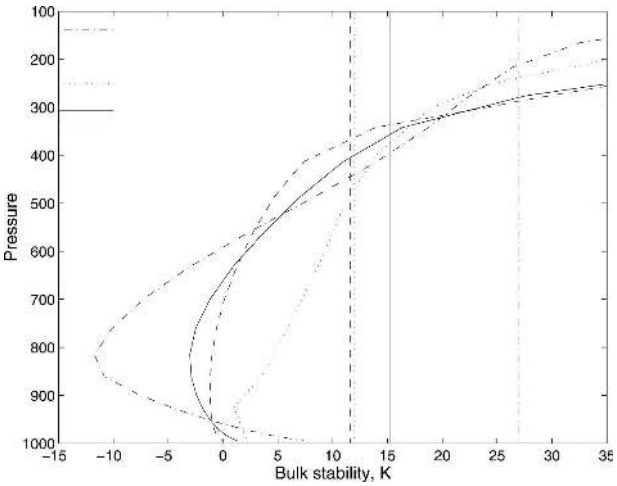

FIG. 13. Bulk moist stability at 45°, with twice the surface moist static energy standard deviation indicated by the dotted lines for the control case (solid), the dry limit (dashed), the 10X case (dash-dot), and the NCEP–NCAR reanalysis data at 45°S, 2000–04 (dotted). The WMO tropopause heights for the simulations are indicated by the horizontal lines on the left axis.

eddy scale, we define the average wavenumber of the disturbances as

$$\overline{k} = \frac{\int kE(k)\,dk}{\int E(k)\,dk}, \tag{24}$$

where $E(k)$ is the spectrum shown in Fig. 14a. We plot the average length scale for this wavenumber

$$\overline{L} = \frac{2\pi a \cos(\theta)}{\overline{k}} \tag{25}$$

in Fig. 14b. In the Tropics the moister cases have smaller scales. However, from the subtropics to the polar regions, the average length scales are very similar. The mean length scale is remarkably constant at around 4000 km over the entire midlatitude and subtropical region for all cases. When averaged over the extratropics, the mean length scale is decreased slightly as the moisture content is increased. In polar regions several of the simulations have larger length scales, but there is sampling error at these latitudes, as can be seen from the asymmetry between hemispheres.

The maximum separation among the three T170 cases in the extratropics occurs at 33°, where the scales decrease with moisture but are still within 7% of each other. The variations with moisture are different at the two resolutions, but they are very small in all cases. The resilience of the length scale to change with moisture is

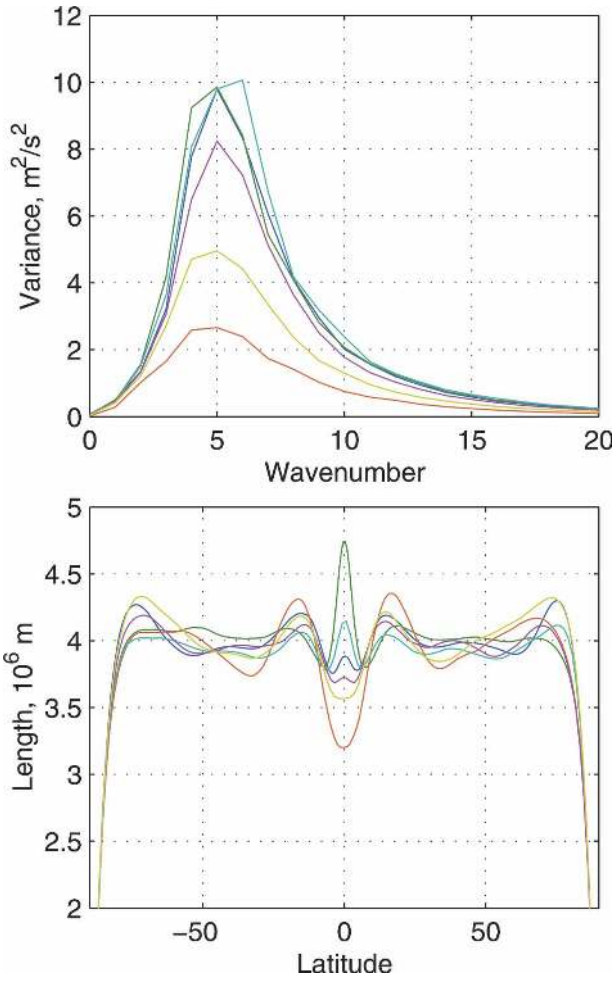

FIG. 14. (top) Zonal wavenumber spectra for $\langle v \rangle$ at 45° latitude for the dry limit (blue), control case (green), and 10X case (red), all at T170 resolution; and the 0.5X case (cyan), 2X case (magenta), and 4X case (yellow), all at T85 resolution. (bottom) Mean length scale $\overline{L}$ as a function of latitude (see text for definition), same color scheme.

quite remarkable given the large changes in static stability.

We compare these mean length scales with two different Rossby radii and a Rhines scale. We define the Rossby radius of deformation using the tropopause height,

$$L_D = 2\pi \frac{NH_T}{f}, \tag{26}$$

where N is the average buoyancy frequency below the WMO tropopause, H_T is the WMO tropopause height discussed above, and f is the local value of the Coriolis parameter; the Rossby radius using a scale height instead of the tropopause height,

$$L_S = 2\pi \frac{NH_s}{f}, \tag{27}$$

where N is calculated as above, and H_s is taken to be 8 km; and a Rhines scale

$$L_\beta = 2\pi \sqrt{\frac{v_{\mathrm{RMS}}}{\beta}}. \tag{28}$$

A comparison of these length scales for the T170 cases is found in Fig. 15; we compare with an area-weighted average of $\overline{L}$ poleward of 25°. The theoretical Rossby radii all increase sharply at the subtropical jet, where there is a jump in the tropopause height and an associated jump in the static stability. Here we focus on the latitudes poleward of the subtropical jet. Clearly the Rossby radii vary much more with moisture than $\overline{L}$. If L_D is used, the predicted increase of length scales at 45° from dry limit to 10X case is a factor of 3.5. Using L_s significantly decreases the scales in the 10X case, but still predicts an increase in scale of 75% from the dry limit to 10X. Since eddies reach significantly higher in the atmosphere as the moisture content is increased (up to the tropopause in all cases), it is presumably unjustified to use an even smaller height scale in the cases with more moisture.

We have computed a moist Rossby radius by substituting a bulk moist stability for the bulk dry stability between the surface and tropopause. It exhibits less variation with moisture than the dry stability Rossby radius, but the predicted change in scale is still too large (and in the wrong direction if we accept the small variations in the T170 cases). For instance, it predicts an increase of length scale of approximately 25% from dry to 10X at 45°. These moist Rossby radii do vary relatively little for all of the cases with intermediate values of moisture (6% at 45°); the dry and 10X cases are the primary outliers. We know of no theoretical justification for this choice in any case. As discussed in the introduction, in the Emanuel et al. (1987) theory for the moist Eady model (see also Zurita-Gotor 2005), the dry stability still controls growth rates and cutoff wavenumbers.

For the dry limit, the Rhines scale is slightly larger than the Rossby radius for all latitudes poleward of the tropopause jump. This difference is small, and we do not see the spectral shapes consistent with an inverse energy cascade that are found in turbulence simulations (not shown). The dry case appears to be broadly consistent with the results of Schneider (2004), in which the static stability adjusts to prevent the supercriticality required to maintain an inverse cascade, and in which there is no separation between the radius of deformation and the Rhines scale. It is possible that our moist

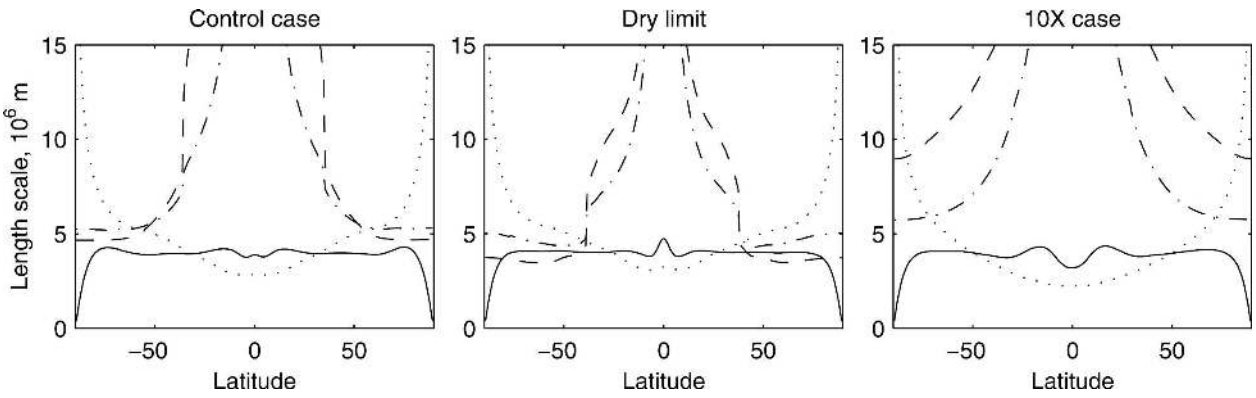

FIG. 15. Comparison of mean length scale (solid) with theoretical predictions of length scales for the control case, dry limit, and 10X case: Rossby radius using tropopause height (dashed), Rossby radius using scale height (dash-dot), and Rhines scale (dotted).

experiments could be interpreted in the same terms, if we knew how to best define an appropriate radius of deformation.

The mean length scales of the GCM $\overline{L}$ are on the same order as the Rhines scale in general (but somewhat smaller poleward of the subtropics). Further, the Rhines scale decreases as moisture is added, which is the same behavior as $\overline{L}$ for the T170 cases. However, at any given latitude the Rhines scale varies much more with moisture than does $\overline{L}$, decreasing by 23% at 45° between the dry limit and the 10X case). Another obvious difference is that, while the observed eddy scale $\overline{L}$ is nearly independent of latitude, the Rhines scale increases strongly with increasing latitude.

We suspect that an important factor in determining the length scales in these experiments is the poleward shift of the jet with increased moisture mentioned in section 3. Whereas at 45° latitude the EKE is significantly smaller for the 10X case, poleward of the EKE maximum these quantities become similar (see Fig. 9). The latitudes of maximum EKE are (46°, 44°, 47°, 50°, 60°, 63°) for $\xi = (0, 0.5, 1, 2, 4, 10)$. When we consider the Rhines scale at the latitude with maximum EKE, then these scales are found to be virtually identical. Usage of this scale in the 10X case increases the length scale both by increasing the value of the velocity variance, and, more importantly, by decreasing the value of β. When this expression is used, the theoretical predictions of the length scale for the T170 cases fall within 1% of each other. For the T85 cases using this scale predicts changes in length of up to 3%, in the correct sense as the observed changes. A summary of all the predicted length scales with ξ, expressed as ratios to the control value, is given in Fig. 16. Additionally, the increase in EKE can explain the increase in scale seen as resolution is increased from T85 to T170. We believe that the Rhines scale at the latitude of maximum EKE provides a plausible explanation for the observed length scales.

The question of whether there is any additional constraint that makes the length scales invariant remains to be answered. One is tempted to think that the eddy scale is just constrained by the geometry, but it changes when one changes the insolation gradient—it decreases by 10% from the control for $\Delta_s = 1.0$ and increases by 8% for $\Delta_s = 1.8$. It can also be increased by reducing the rotation rate.

6. Conclusions

We have presented a moist general circulation model with simplified physical parameterization schemes, de-

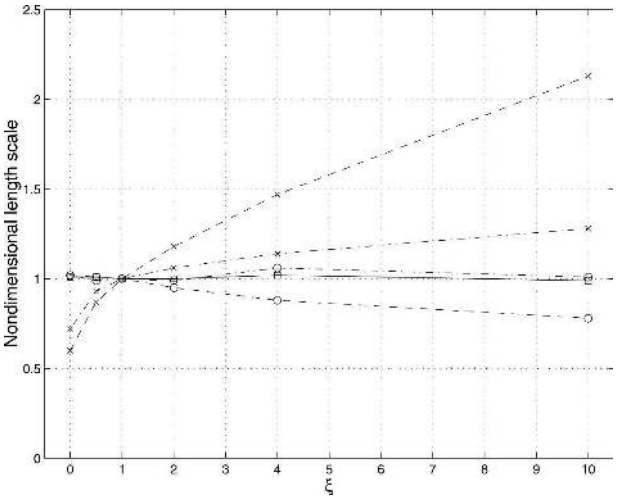

FIG. 16. Moisture dependence of all length scales discussed in the text, normalized by their respective control values: $\overline{L}$ (solid line with □), L_D at 45° (dashed line with ×), L_S at 45° (dash-dot with ×), L_β at 45° (dashed line with ○), and L_β at latitude of maximum EKE (dash-dot with ○).

signed to bridge the gap between GCMs and idealized dry models. Perhaps the key simplification is that moisture does not affect radiative transfer, so that we can isolate the dynamical effects of changes in water vapor content from its radiative effects. While our simplifications are unlikely to be ideal, we believe that models of this level of complexity can be useful for a wide variety of studies, if only because they should be more easily reproducible than full GCMs. Since our framework includes upward and downward radiative fluxes and a boundary layer scheme, the model can be built up systematically to a full GCM. We have developed a version of this model with a simplified Betts–Miller convection scheme which creates a more realistic tropical climate, and allows for the study of the sensitivity of the atmospheric general circulation to convection scheme parameters (Part II). The model with the convection scheme additionally has less sensitivity to model resolution in the Tropics (it is essentially converged at T42).

In this study, we have varied the model's moisture content over a wide range to investigate the effect of moisture on the static stability. As moisture is increased, the dry static stability increases drastically, while the moist stability increases gradually, consistent with an increased surface variance of moist static energy, as postulated by Juckes (2000). The moist stability is also found to increase as insolation gradients are increased, again consistent with increased surface variance.

The effect of convection can be directly diagnosed in the dry case, where the planetary boundary layer depth indicates the vertical extent of convection. By examining PDFs of this quantity, we find that convection often reaches the vicinity of the tropopause in midlatitudes. Below the tropopause, a region of mean stability exists over which the boundary layer depth varies in time. The stability in this region increases as the variance of the boundary layer depth increases. This layer of mean stability accounts for the bulk stability of the atmosphere (the difference in static energy between surface and tropopause). Although there is no equivalent diagnostic for the moist cases, the values of the moist stability and its variation with moisture and insolation gradient suggests that convection exerts a similar control in all cases.

Since there is such a large increase in dry stability as moisture is increased, and since eddy length scales are often thought of as controlled by the radius of deformation, which is proportional to this stability, we have also focused on the changes in eddy length scales. The length scales change remarkably little with moisture. The small changes that do occur are in the opposite sense as expected: a slight decrease of length scales with increasing moisture. In an attempt to explain this insensitivity, we find that the the Rhines scale at the latitude of maximum eddy kinetic energy provides an excellent fit to the length scale. We do not claim that this alone is a satisfying explanation, since the invariance of the length scale then appears as an accident, controlled in part by the large poleward shift of the jet and the eddy activity as moisture is increased.

In Part II, we expand upon this theory, focusing on the latitude of maximum eddy kinetic energy and its value at this latitude. These are then used in an energy balance model that predicts the meridional moist static energy fluxes as moisture content varies as well as the bulk moist stability of the model atmosphere.

REFERENCES

Barry, L., G. C. Craig, and J. Thuburn, 2002: Poleward heat transport by the atmospheric heat engine. *Nature,* **415,** 774–777.

Collela, P., and P. R. Woodward, 1984: The Piecewise Parabolic Method (PPM) for gas-dynamical simulations. *J. Comput. Phys.,* **54,** 174–201.

Donner, L. J., 1986: Sensitivity of the thermal balance in a general circulation model to a parameterization for cumulus convection with radiatively interactive clouds. *J. Atmos. Sci.,* **43,** 2277–2288.

——, H.-L. Kuo, and E. J. Pitcher, 1982: The significance of thermodynamic forcing by cumulus convection in a general circulation model. *J. Atmos. Sci.,* **39,** 2159–2181.

Emanuel, K. A., 1988: Observational evidence of slantwise convective adjustment. *Mon. Wea. Rev.,* **116,** 1805–1816.

——, M. Fantini, and A. J. Thorpe, 1987: Baroclinic instability in an environment of small stability to slantwise moist convection. Part I: Two-dimensional models. *J. Atmos. Sci.,* **44,** 1559–1573.

Franzke, C., 2002: Dynamics of low-frequency variability: Barotropic mode. *J. Atmos. Sci.,* **59,** 2897–2909.

——, S. Lee, and S. B. Feldstein, 2004: Is the North Atlantic Oscillation a breaking wave? *J. Atmos. Sci.,* **61,** 145–160.

Frierson, D. M. W., I. M. Held, and P. Zurita-Gotor, 2006: A gray-radiation aquaplanet moist GCM. Part II: Energy transports in altered climates. *J. Atmos. Sci.,* in press.

Green, J. S., 1970: Transfer properties of the large scale eddies and the general circulation of the atmosphere. *Quart. J. Roy. Meteor. Soc.,* **96,** 157–185.

Harnik, N., and E. K. M. Chang, 2004: The effects of variations in jet width on the growth of baroclinic waves: Implications for midwinter Pacific storm track variability. *J. Atmos. Sci.,* **61,** 23–40.

Haynes, P., J. Scinocca, and M. Greenslade, 2001: Formation and maintenance of the extratropical tropopause by baroclinic eddies. *Geophys. Res. Lett.,* **28,** 4179–4182.

Held, I. M., 1982: On the height of the tropopause and the static stability of the troposphere. *J. Atmos. Sci.,* **39,** 412–417.

——, and M. J. Suarez, 1994: A proposal for the intercomparison of the dynamical cores of atmospheric general circulation models. *Bull. Amer. Meteor. Soc.,* **75,** 1825–1830.

——, and V. D. Larichev, 1996: A scaling theory for horizontally homogeneous, baroclinically unstable flow on a beta plane. *J. Atmos. Sci.,* **53,** 946–952.

Juckes, M. N., 2000: The static stability of the midlatitude troposphere: The relevance of moisture. *J. Atmos. Sci.,* **57,** 3050–3057.

Kushner, P. J., and L. M. Polvani, 2004: Stratosphere–troposphere coupling in a relatively simple AGCM: The role of eddies. *J. Climate,* **17,** 629–639.

Lapeyre, G., and I. M. Held, 2004: The role of moisture in the dynamics and energetics of turbulent baroclinic eddies. *J. Atmos. Sci.,* **61,** 1693–1710.

Rhines, P. B., 1975: Waves and turbulence on a beta-plane. *J. Fluid Mech.,* **69,** 417–443.

Schneider, T., 2004: The tropopause and the thermal stratification in the extratropics of a dry atmosphere. *J. Atmos. Sci.,* **61,** 1317–1340.

Seager, R., R. Murtugudde, N. Naik, A. Clement, N. Gordon, and J. Miller, 2003: Air–sea interaction and the seasonal cycle of the subtropical anticyclones. *J. Climate,* **16,** 1948–1966.

Stone, P. H., 1972: A simplified radiative-dynamical model for the static stability of rotating atmospheres. *J. Atmos. Sci.,* **29,** 405–418.

Thuburn, J., and G. C. Craig, 1997: GCM tests of theories for the height of the tropopause. *J. Atmos. Sci.,* **54,** 869–882.

Troen, I., and L. Mahrt, 1986: A simple model of the atmospheric boundary layer: Sensitivity to surface evaporation. *Bound.-Layer Meteor.,* **37,** 129–148.

Williams, G., 2003: Barotropic instability and equatorial superrotation. *J. Atmos. Sci.,* **60,** 2136–2152.

Zurita-Gotor, P., 2005: Updraft/downdraft constraints for moist baroclinic modes and their implications for the short-wave cutoff and maximum growth rate. *J. Atmos. Sci.,* **62,** 4450–4458.